Nanoscale

PAPER

View Article Online
View Journal | View Issue

Check for updates

Cite this: *Nanoscale*, 2023, **15**, 2779

Two-dimensional MBenes with ordered metal vacancies for surface-enhanced Raman scattering†

Leilei Lan,[a,b] Xingce Fan,[b] Caiye Zhao,[a] Juan Gao,[a] Zhongwei Qu,[a] Wenzhe Song,[b] Haorun Yao,[b] Mingze Li[b] and Teng Qiu*[b,c]

As an emerging class of two-dimensional (2D) materials, MBenes show enormous potential for optoelectronic applications. However, their use in molecular sensing as surface-enhanced Raman scattering (SERS)-active material is unknown. Herein, for the first time, we develop a brand-new high-performance MBene SERS platform. Ordered vacancy-triggered highly sensitive SERS platform with outstanding signal uniformity based on a 2D $Mo_{4/3}B_2$ MBene material was designed. The 2D $Mo_{4/3}B_2$ MBene presented superior SERS activity to most of the semiconductor SERS substrates, showing a remarkable Raman enhancement factor of 3.88×10^6 and an ultralow detection limit of 1×10^{-9} M. The underlying SERS mechanism is revealed from systematic experiments and density functional theory calculations that the ultrahigh SERS sensitivity of 2D $Mo_{4/3}B_2$ MBene is derived from the efficient photoinduced charge transfer process between MBene substrates and adsorbed molecules. The abundant electronic density of states near the Fermi level of 2D $Mo_{4/3}B_2$ MBene enables its Raman enhancement by a factor of 100 000 times higher than that of the bulk MoB. Consequently, the 2D $Mo_{4/3}B_2$ MBene could accurately detect various trace chemical analytes. Moreover, with ordered metal vacancies in the 2D $Mo_{4/3}B_2$ MBene, uniform charge transfer sites are formed, resulting in an outstanding signal uniformity with a relative standard deviation down to 6.0%. This work opens up a new horizon for the high-performance SERS platform based on MBene materials, which holds great promise in the field of chemical sensing.

Received 9th November 2022,
Accepted 5th January 2023

DOI: 10.1039/d2nr06280a

rsc.li/nanoscale

Published on 06 Genver 2023. Downloaded on 2025-08-25 06:33:52.

1. Introduction

As a powerful molecular fingerprinting technique with ultrahigh sensitivity, non-destructiveness, and label-free detection, surface-enhanced Raman scattering (SERS) has been widely applied in environmental science, biomedicine, molecular analysis, and catalytic mechanism exploration.[1–5] Normally, there are two widely accepted SERS enhancement mechanisms, the electromagnetic mechanism (EM) and the chemical mechanism (CM). The former mainly originates from a magnifying local electromagnetic field depending on localized surface plasmon resonance (LSPR), while the latter benefits from the charge transfer (CT) between the substrates and the adsorbed molecules.[4,5] In the SERS measurement, substrate materials play an important role. Traditionally, EM-based noble metals (*i.e.*, Au and Ag) have been dominant as SERS-active materials because of their ultra-high sensitivity even at single-molecule level detection. Nevertheless, some inevitable shortcomings including expensive price, poor signal uniformity, lack of stability, and complicated "hotspots" regulation, greatly restrict the large-scale application of noble metal SERS substrates. In contrast, noble-metal-free materials have the advantages of abundant sources, tunable band structure, good chemical stability, superior biocompatibility, and unique selectivity to target molecules,[6,7] which could effectively make up for the shortcomings of noble metals and greatly broaden the application of SERS.

Recently, the discovery of CM-based two-dimensional (2D) SERS materials opens a new prospect for SERS research. 2D materials possess atomically flat surfaces, large specific surface areas, and insufficient coordination number of surface atoms, making it more likely that surface atoms and adsorbed molecules are combined and further form uniformly distributed surface complexes, which induce efficient photoinduced charge transfer (PICT) process and good signal uniformity.[8] So far, a series of 2D SERS-active materials, including graphene,[9] transition metal dichalcogenides,[8,10] transition metal oxides,[11,12] metal–organic frameworks,[13] and transition metal carbides/nitrides (MXenes)[14,15] have been developed. To

[a]*School of Mechanics and Optoelectronic Physics, Anhui University of Science and Technology, Huainan 232001, China*
[b]*School of Physics, Southeast University, Nanjing 211189, China. E-mail: tqiu@seu.edu.cn*
[c]*Center for Flexible RF Technology, Frontiers Science Center for Mobile Information Communication and Security, Southeast University, Nanjing 210096, China*
† Electronic supplementary information (ESI) available. See DOI: https://doi.org/10.1039/d2nr06280a

Published on 06 Genver 2023. Downloaded on 2025-08-25 06:33:52.

further improve their SERS performance, some enhancement strategies such as heterojunction engineering,[16] phase transition,[10] amorphization treatment,[12] defect engineering,[17] molecular enrichment,[18] and thickness adjustment[19] have been explored. Among them, defect engineering is widely used in the research of 2D materials, which provides an effective strategy for the activation and promotion of intrinsic SERS activity. In general, defect engineering breaks the periodic arrangement of atoms, producing point defects or higher dimensional disorder.[20] The introduction of defects in 2D materials would change their surface properties, band structures, and density of states (DOS), leading to strong surface interactions, light-trapping capability, or charge transport efficiency, bringing about a direct effect on the SERS performance of 2D materials.[21] For example, Zhao *et al.* demonstrated that ultrathin 2D nanostructures with surface defects could be advantageous in promoting SERS sensitivity.[11] Seo *et al.* reported that single-atom vanadium-doped 2D $ReSe_2$ platform could achieve attomolar level molecular sensing capability.[22] Nb, Re dual-doped WSe_2 exhibits ultra-high SERS sensitivity with a femtomolar level detection limit.[23] However, since these defects are usually either produced inadvertently or formed in macroscopic processes, leading their types and extents are not highly controlled. The disorder defects with uneven distribution can improve the SERS sensitivity but cause poor signal uniformity. Therefore, large-scale control of the ordered defects at the atomic level is of great significance for simultaneously improving the SERS sensitivity and signal uniformity of 2D materials.

As an emerging class of 2D materials, MBenes (transition metal borides) have been theoretically predicted first and experimentally synthesized in the past few years.[24–31] In general, MBenes are the derivative of ternary or quaternary MAB phases (where M is an early transition metal, A is an A-group element, and B is a boron element), which possess diverse structures and stoichiometries. Thus far, some types of MBenes, such as MoB,[26] TiB,[27] CrB,[29] and ZrB_2,[30] have been synthesized by selective etching of element A from their MAB phases. These 2D MBenes featuring excellent electrical conductivity, large surface areas, high mechanical strength/stability, and outstanding thermal conductivity, have been extensively studied in the fields of batteries, catalysts, and biomedicine.[24,28,30,31] Especially, similar to the SERS-active MXene materials, MBenes show metallic behavior, which may produce an efficient PICT process between the Fermi level of MBenes and the molecular level of the probe molecules. Moreover, MBenes possess multiple types of crystallographic arrangements and structural transformations, making them more likely to optimize their SERS performance. These properties inspired us to further study 2D MBene materials as they may become an innovative SERS platform.

Herein, ordered vacancy-triggered highly sensitive MBene-based SERS substrate with superior signal uniformity was developed. 2D $Mo_{4/3}B_2$ MBene with ordered metal vacancies was fabricated by selectively etching both the Al and Y atoms from an in-plane chemically ordered $(Mo_{2/3}Y_{1/3})_2AlB_2$. It is demonstrated that 2D $Mo_{4/3}B_2$ Mbene could be used as a SERS-active material, which has not been reported before. Furthermore, we verified that high SERS activity of 2D $Mo_{4/3}B_2$ Mbene substrate was achieved based on the efficient PICT process between the probe molecules and MBene substrates. Compared with bulk MoB, 2D $Mo_{4/3}B_2$ MBene has more abundant DOS near the Fermi level, thereby improving the SERS sensitivity by up to 100 000 times. Consequently, 2D $Mo_{4/3}B_2$ MBene could accurately detect various chemical analytes at the trace level. In addition, 2D $Mo_{4/3}B_2$ MBene substrate also shows excellent air-stability (over one month), good signal uniformly with a relative standard deviation (RSD) of 6.0%, and superior quantitative analysis ability with a coefficient of determination R^2 of 0.996, which are essential for the practical applications. Our work enriches the diversity of SERS-active materials and may inspire more researchers to explore other 2D MBenes with excellent SERS performance.

2. Results and discussion

2.1 Synthesis and characterization of the 2D $Mo_{4/3}B_2$ MBene

2D $Mo_{4/3}B_2$ MBene was synthesized by a two-step chemical exfoliation process (Fig. 1a). Firstly, hydrofluoric acid (HF) was used to etch Al and Y atoms from $(Mo_{2/3}Y_{1/3})_2AlB_2$. The $Mo_{4/3}Y_{2/3}AlB_2$ is a structure with space group $R\bar{3}m$ (no. 166), which displays the characteristic in-plane chemical order of Mo and Y and Kagoméordering of the Al atoms.[32] Then, etched MBene powder was further delaminated in tetrabutylammonium hydroxide (TBAOH) aqueous solution to reduce the vertical dimension. Because of the ordered arrangements of Mo and Y atoms in the original $(Mo_{2/3}Y_{1/3})_2AlB_2$ MAB phase, highly ordered metal vacancies are formed after the selective removal of Y atoms.[33–35] The preparation methods are detailed in the experimental section. Fig. 1b shows the XRD patterns of $(Mo_{2/3}Y_{1/3})_2AlB_2$ MAB phase and $Mo_{4/3}B_2$ MBene, in which all the diffractive peaks belonging to the MAB phase disappeared completely, and a new broadened (00l) peak at 7.3° (d-spacing = 1.21 nm) appeared, implying the successful synthesis of 2D MBene.[33] This low-angled (00l) peak is usually observed in 2D MXenes prepared by the HF-etched MAX phase.[36,37] The element composition and chemical states of $(Mo_{2/3}Y_{1/3})_2AlB_2$ MAB phase and 2D $Mo_{4/3}B_2$ MBene were investigated using X-ray photoelectron spectroscopy (XPS). In the survey XPS survey spectra (Fig. 1c), the photoemission of Mo, B, Al, Y, O, and C elements was observed in the $(Mo_{2/3}Y_{1/3})_2AlB_2$ MAB phase. After the HF etching treatment, the photoemission from the Y 3p and Al 2p orbitals disappeared. The removal of Al atoms was further confirmed by the high-resolution XPS spectrum of Al 2p (Fig. 1d). The XPS results indicate that the Y and Al atoms were effectively removed from the $(Mo_{2/3}Y_{1/3})_2AlB_2$ MAB phase. In addition, the surface terminations of the -O, -OH, and -F functional groups were also observed on 2D $Mo_{4/3}B_2$. In Fig. 1e, the Mo 3d photoemission spectrum of 2D $Mo_{4/3}B_2$ MBene can be fitted with four pairs of deconvoluted peaks in the range of 226.0 to 237.0 eV, which

 This journal is © The Royal Society of Chemistry 2023

Published on 06 Genver 2023. Downloaded on 2025-08-25 06:33:52.

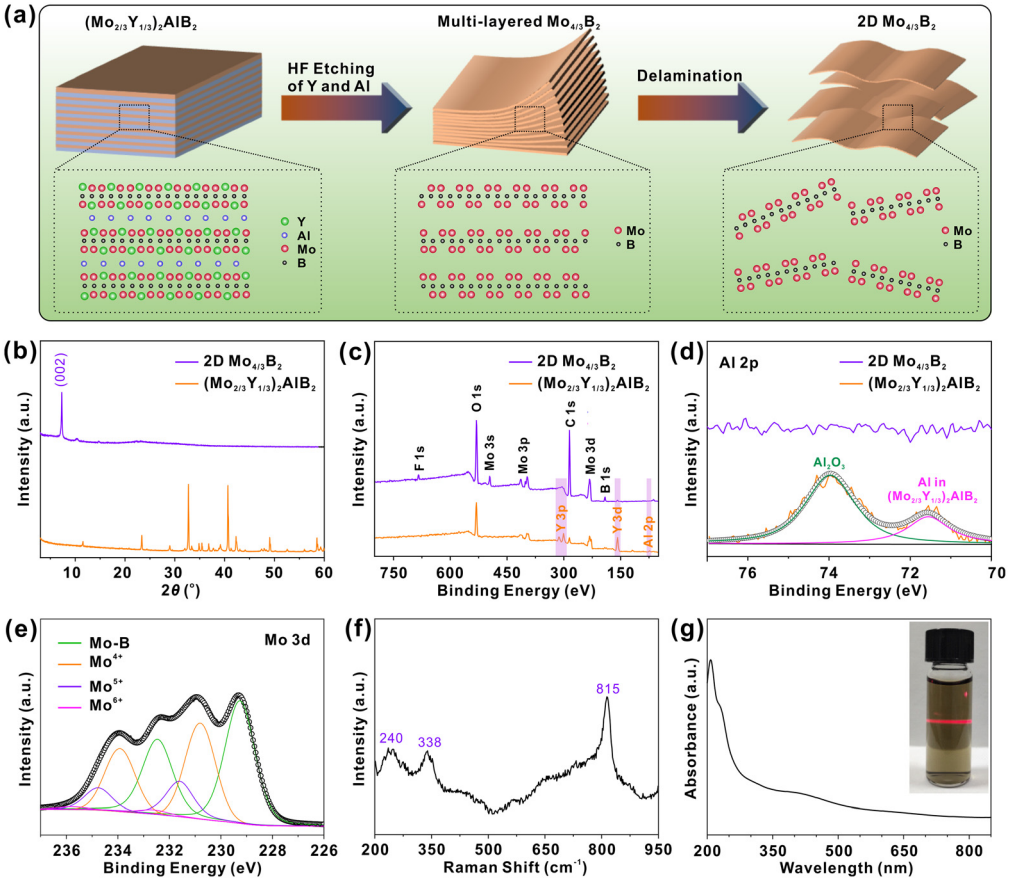

Fig. 1 Synthesis and characterization of 2D $Mo_{4/3}B_2$ MBene. (a) Schematics of the synthesis of 2D $Mo_{4/3}B_2$ MBene by a two-step chemical exfoliation process. (b and c) XRD patterns and XPS spectra of $(Mo_{2/3}Y_{1/3})_2AlB_2$ MAB phase and 2D $Mo_{4/3}B_2$ MBene. (d and e) Al 2p and Mo 3d XPS spectra of 2D $Mo_{4/3}B_2$ MBene. (f) Raman spectrum of 2D $Mo_{4/3}B_2$ MBene. (g) UV-vis absorption spectrum of 2D $Mo_{4/3}B_2$ MBene. Inset: a photograph of 2D MBene dispersion.

are attributed to Mo-B (229.3, 232.5 eV), Mo^{4+} (230.8, 233.9 eV), Mo^{5+} (231.6, 234.8 eV) and Mo^{6+} (232.6, 235.8 eV). The Raman spectrum of 2D $Mo_{4/3}B_2$ MBene was measured, as shown in Fig. 1f, where three observed Raman peaks at 240, 338, and 815 cm^{-1} are assigned to molybdenum boride.[38,39] The Raman peaks at 240 and 338 cm^{-1} originate from the E_{1g} and E^1_{2g} vibration modes of molybdenum boride and the peak at 815 cm^{-1} is ascribed to the vibration mode of the Mo–B band. Fig. 1g shows the UV-vis absorption spectrum of 2D $Mo_{4/3}B_2$ MBene dispersion, in which, a distinct absorption peak at ~215 nm was observed and ascribed to the presence of surface functional groups.[14] The inset of Fig. 1g shows a photograph of 2D Mbene dispersion, which appears in brown color and is accompanied by an obvious Tyndall effect.

Scanning electron microscope (SEM), transmission electron microscope (TEM), and atomic force microscope (AFM) were used to examine the sample morphologies. The SEM image of $(Mo_{2/3}Y_{1/3})_2AlB_2$ is shown in Fig. 2a, in which a 3D particle-like structure with several micrometers is observed. After the HF etching treatment, the compact layers are expanded and the multi-layered morphology is formed (Fig. 2b and c). Furthermore, the few-layered structure of delaminated 2D $Mo_{4/3}B_2$ MBene with a lateral size of several hundred nanometers is observed (Fig. 2d), which is similar to the morphologies of typical MXenes.[14,36] The AFM image and the corresponding line profile of the few-layered $Mo_{4/3}B_2$ MBene are presented in Fig. 2e and f, further revealing the 2D feature of $Mo_{4/3}B_2$ MBene with a thickness of only ~4 nm. The SEM image and the corresponding elemental mapping images of the 2D $Mo_{4/3}B_2$ MBene substrate are shown in Fig. 2g, where a smooth morphology of the 2D $Mo_{4/3}B_2$ MBene is observed and the Mo, B, F, and O elements are homogeneously distributed in the sample.

2.2 SERS performance of the 2D $Mo_{4/3}B_2$ MBene substrate

The SERS performance of 2D $Mo_{4/3}B_2$ MBene was investigated by adopting Rhodamine 6G (R6G) as a probe molecule under the illumination of 532 nm. In the Raman spectrum of R6G (1×10^{-6} M) adsorbed on 2D $Mo_{4/3}B_2$ MBene (Fig. 3a), four characteristic Raman peaks located at P1 (612 cm^{-1}), P2 (773 cm^{-1}), P3 (1360 cm^{-1}), and P4 (1650 cm^{-1}) can be clearly observed, among which, P1 and P2 are assigned to the in-plane and out-of-plane bending modes of the aromatic C–H, respectively, and P3 and P4 correspond to the stretching vibrations of the aromatic C–C.[40] While no Raman signal of

Published on 06 Genver 2023. Downloaded on 2025-08-25 06:33:52.

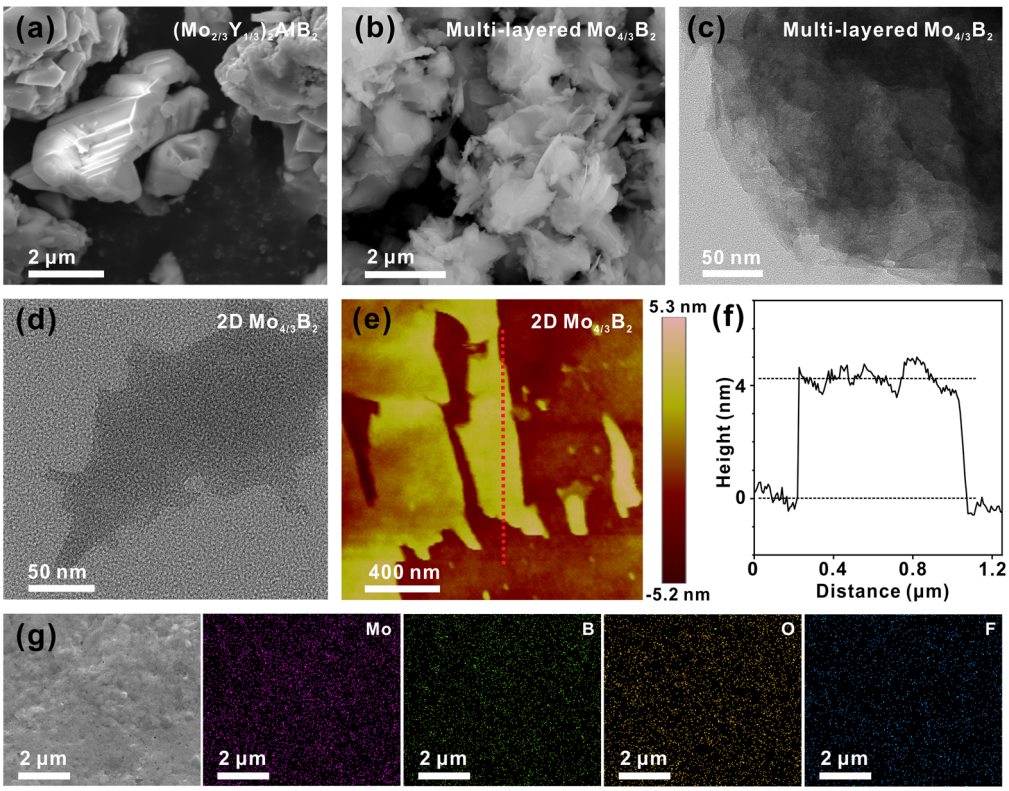

Fig. 2 Characterizations of the surface morphologies of MAB, multi-layered, and 2D $Mo_{4/3}B_2$ MBenes. (a and b) SEM images of $(Mo_{2/3}Y_{1/3})_2AlB_2$ and multi-layered $Mo_{4/3}B_2$ MBene. (c and d) TEM images of multi-layered and 2D $Mo_{4/3}B_2$ MBenes. (e) AFM image of 2D $Mo_{4/3}B_2$ MBene. (f) Line profile across the dashed line in the image (e). (g) SEM image and the corresponding elemental mapping images of the 2D $Mo_{4/3}B_2$ MBene substrate.

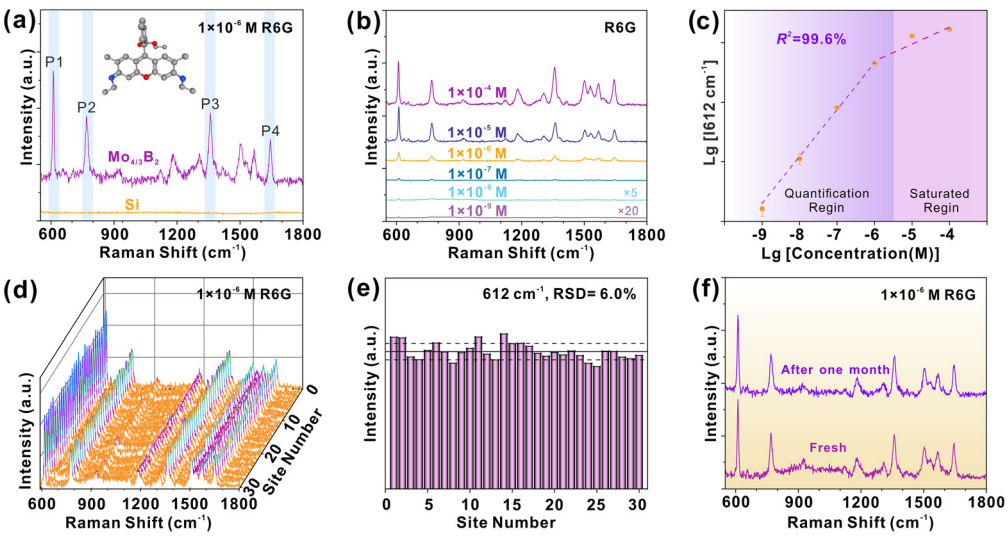

Fig. 3 SERS performance of 2D $Mo_{4/3}B_2$ MBene substrate. (a) Raman spectra of R6G (1×10^{-6} M) adsorbed on bare Si and 2D $Mo_{4/3}B_2$ MBene substrates. (b) Raman spectra of R6G at different concentrations (1×10^{-4} to 1×10^{-9} M) adsorbed on 2D $Mo_{4/3}B_2$ MBene substrates. (c) The logarithm of the integral Raman intensity at 612 cm^{-1} as a function of molecular concentration, and corresponding fitting curves. (d) Raman spectra of R6G (1×10^{-6} M) acquired from 30 random sites on the 2D $Mo_{4/3}B_2$ MBene substrate. (e) The intensity columns of 612 cm^{-1} peaks derived from (d). (f) Raman spectra of R6G (1×10^{-6} M) acquired on 2D $Mo_{4/3}B_2$ substrates before and after storing in the air for one month.

R6G can be observed on bare Si, excluding the Raman enhancement effect of the bare Si substrate. It is for the first time to demonstrate 2D $Mo_{4/3}B_2$ MBene as a SERS-active material. The detection limit was evaluated by immersing 2D $Mo_{4/3}B_2$ MBene substrates into R6G solutions with different concentrations (1×10^{-4} to 1×10^{-9} M) (Fig. 3b). The Raman

 This journal is © The Royal Society of Chemistry 2023

Published on 06 Genver 2023. Downloaded on 2025-08-25 06:33:52.

peaks of R6G can still be detected even at a concentration of as low as 1×10^{-9} M, indicating that 2D $Mo_{4/3}B_2$ MBene is an ultrasensitive SERS platform. The corresponding Raman enhancement factor (EF) was estimated to be 3.88×10^6 at the concentration of 1×10^{-9} M, which is comparable to those reported for high-performance semiconducting or even noble metal SERS platforms (Table S1 in the ESI†).[9,12,14,15,41–50] Detailed calculation of the Raman EF is shown in Section S1 in the ESI.† Fig. 3c presents the working curve of the Raman intensity with R6G concentration in the logarithmic scale. A saturated region is distinguished at high R6G concentrations ($>1 \times 10^{-6}$ M). Besides, the working curve of the Raman intensity *versus* R6G concentration was fitted as a linear function ($R^2 = 0.996$) over the concentration range of 1×10^{-6} M to 1×10^{-9} M, which laid the foundation for the potential application of quantitative detection. Next, 30 random points were tested on the 2D $Mo_{4/3}B_2$ MBene substrate (Fig. 3d) to investigate their SERS signal uniformity. By monitoring the Raman intensities of peak P1, the RSD was calculated to be 6.0% (Fig. 3e), which is much lower than those of the tantalum oxide with disordered oxygen vacancies (13.5%),[46] plasmonic gold nanorods (22%),[51] and atomically thin $TaSe_2$ film (11.8%).[47] The relatively low RSD value proves the excellent signal uniformity of 2D $Mo_{4/3}B_2$ MBene. Generally, SERS substrates require the homogeneity of CT sites or plasmonic "hotspots" to generate superior signal uniformity. In this work, 2D $Mo_{4/3}B_2$ MBene substrates showed smooth surface morphology (Fig. 2g and Fig. S1 in the ESI†) and the ordered metal vacancy sites, which guarantee the homogeneity of the CT sites and enable ideal SERS signal uniformity. The 2D $Mo_{4/3}B_2$ MBene also possesses high air stability and its SERS activity remains virtually unchanged after one month of storage in air (Fig. 3f). The 2D $Mo_{4/3}B_2$ MBene substrate can also be used to detect a series of chemicals, such as fuchsin acid (FA), crystal violet (CV), methylene blue (MB), malachite green (MG), and rhodamine B (RhB), and brilliant green (BG) (Fig. 4), among which CV and MG are both the banned fish drugs for their adverse effects on the health and the environment.[8] The detection limits of FA, CV, MB, MG, RhB, and BG were tested as low as 1×10^{-7}, 1×10^{-8}, 1×10^{-6}, 1×10^{-8}, 1×10^{-6}, and 1×10^{-7} M, respectively, demonstrating the enormous potential of 2D $Mo_{4/3}B_2$ MBene in practical applications. In short, all the results clearly certify that the 2D $Mo_{4/3}B_2$ MBene substrate is an innovative and high-performance SERS platform.

2.3 Raman enhancement mechanism of 2D $Mo_{4/3}B_2$ MBene substrate

To reveal the Raman enhancement mechanism of 2D $Mo_{4/3}B_2$ MBene, experiments and density functional theory (DFT) calculations were performed. Generally, EM contribution originates from the enhanced local electromagnetic field, which is generated by the LSPR effect.[43] However, the LSPR band was not observed in the UV-vis absorption spectrum (Fig. 1g) and the planar surface morphologies of 2D $Mo_{4/3}B_2$ MBene substrates (Fig. 2g and Fig. S1 in the ESI†) should not induce LSPR effect as well, suggesting the EM mechanism can be excluded. Therefore, we speculated that the underlying Raman enhancement mechanism of 2D $Mo_{4/3}B_2$ MBene should be CM-dominated. Compared with the UV-vis absorption spectrum of R6G, the absorption peak of $Mo_{4/3}B_2$-R6G shifts (Fig. 5a), indicating the chemisorption of R6G on 2D $Mo_{4/3}B_2$ surface and the CT behavior at the $Mo_{4/3}B_2$-R6G interface.[44] The shifted absorption band of R6G originates from the strong dipole interaction and the quasi-covalent bond interaction between $Mo_{4/3}B_2$ MBene and R6G, which could offer additional routes of charge exchange and greatly increase the Raman scattering cross-section of the adsorbed molecules consequently. A similar phenomenon could also be observed in

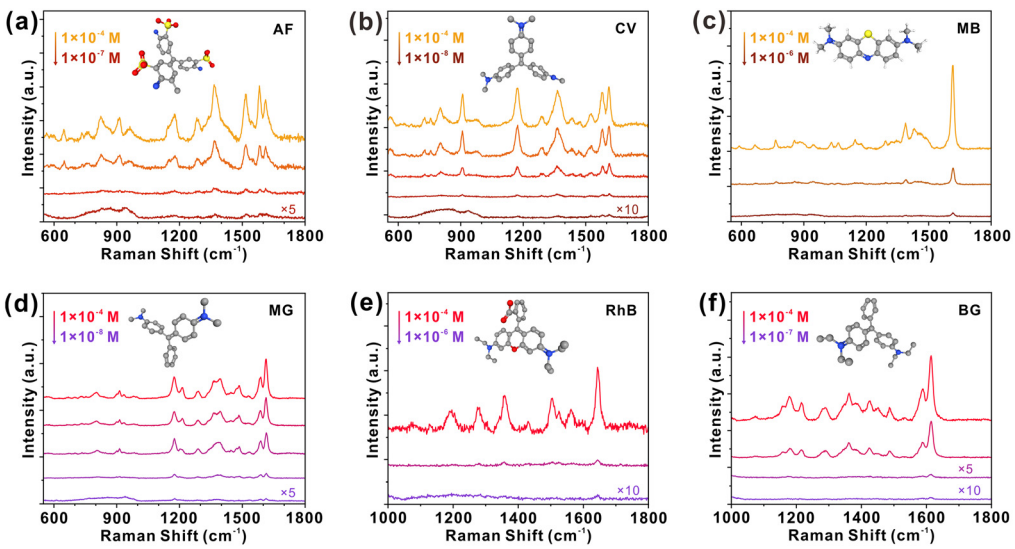

Fig. 4 Raman spectra of the detected chemicals by using 2D $Mo_{4/3}B_2$ MBene SERS substrates. Raman spectra of (a) AF, (b) CV, (c) MB, (d) MG, (e) RhB, and (f) BG molecules with different concentrations adsorbed on the 2D $Mo_{4/3}B_2$ MBene substrates.

Published on 06 Genver 2023. Downloaded on 2025-08-25 06:33:52.

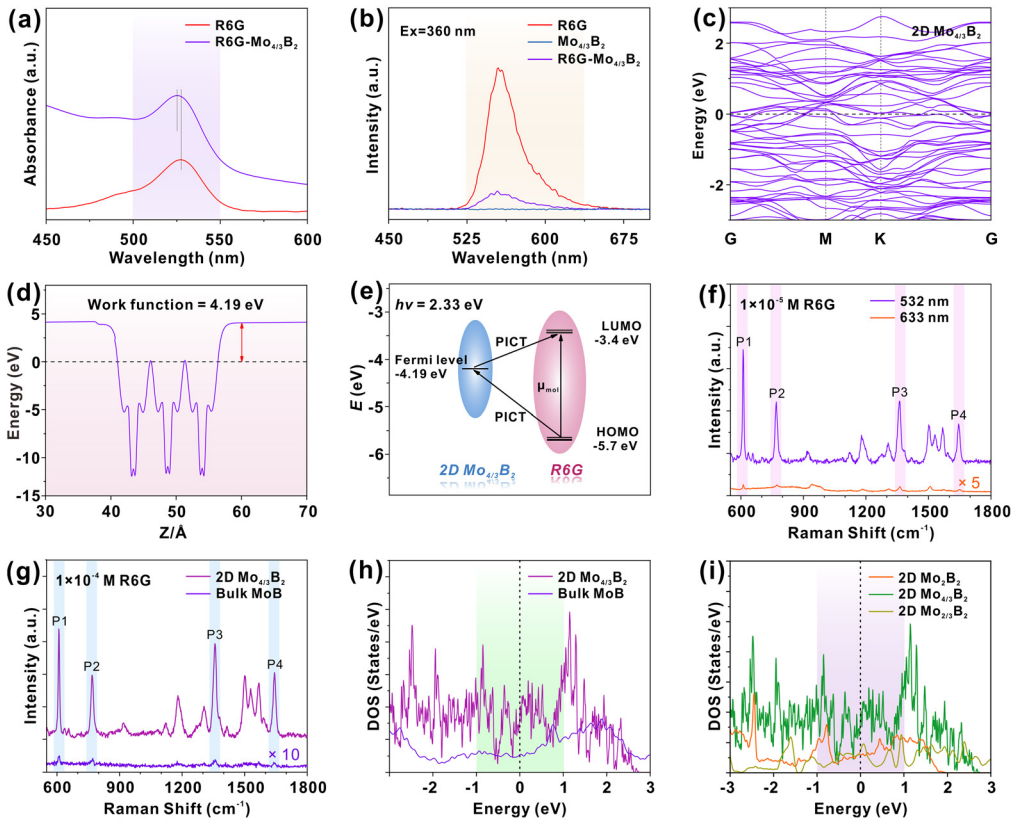

Fig. 5 Raman enhancement mechanism of 2D $Mo_{4/3}B_2$ MBene substrate. (a) UV-vis absorption spectra of R6G and $Mo_{4/3}B_2$-R6G. (b) PL spectra of R6G, $Mo_{4/3}B_2$ and R6G-$Mo_{4/3}B_2$. (c and d) The DFT calculations of electronic band structure and work function of 2D $Mo_{4/3}B_2$. (e) The schematic energy level diagram of the $Mo_{4/3}B_2$-R6G system under the illumination of 532 nm (2.33 eV). (f) Raman spectra of R6G (1×10^{-5} M) adsorbed on 2D $Mo_{4/3}B_2$ measured using the laser at 532 and 633 nm wavelengths. (g) Raman spectra of R6G (1×10^{-4} M) adsorbed on bulk MoB and 2D $Mo_{4/3}B_2$. (h) The DFT calculations of the DOS of bulk MoB and 2D $Mo_{4/3}B_2$. (i) The DFT calculations of the DOS of 2D Mo_2B_2 and $Mo_{4/3}B_2$ and $Mo_{2/3}B_2$.

CV-$Mo_{4/3}B_2$ system (Fig. S2 in the ESI†). Fig. 5b shows the photoluminescence (PL) spectra of R6G, $Mo_{4/3}B_2$, and $Mo_{4/3}B_2$-R6G, where the PL quenching of R6G was observed upon the addition of $Mo_{4/3}B_2$. The quenched PL evidences the efficient CT process between R6G and 2D $Mo_{4/3}B_2$ MBene.[47] Besides, 2D $Mo_{4/3}B_2$ MBene does not show PL emission, which provides an ideal SERS platform with a weak background (Fig. S3 in the ESI†). The CT degree of R6G (1×10^{-6} M) on 2D $Mo_{4/3}B_2$ MBene was estimated to be 0.64, further indicating the CM-dominated feature of this system.[11] For the detailed calculations of the CT degree please refer to section S2 in the ESI.† Furthermore, the electronic band structure and the DOS of 2D $Mo_{4/3}B_2$ MBene are shown in Fig. 5c and Fig. S4 in the ESI† respectively, confirming its metallic character. Metallic $Mo_{4/3}B_2$ shows abundant electronic DOS near the Fermi level such that the possible PICT processes would occur between the Fermi level of $Mo_{4/3}B_2$ MBene and the molecule energy levels. Based on the DFT calculations (Fig. 5d), the Fermi level of $Mo_{4/3}B_2$ is located at −4.19 eV with respect to the vacuum level. Taking R6G as a probe molecule, its highest occupied molecule orbital (HOMO) and lowest unoccupied molecule orbital (LUMO) levels are located at −5.70 eV and −3.40 eV, respectively. In general, the polarization tensor (α) can be expressed as $\alpha = A + B + C$, where A term represents the contributions from the resonance Raman scattering, and B and C terms are relevant to the substrate-to-molecule and molecule-to-substrate CT transitions. As shown in Fig. 5e, the molecular resonance (A-term) would be induced under laser excitation of 532 nm because the energy gap between the HOMO and LUMO levels of the R6G molecule (2.30 eV) is close to the incident photon energy (2.33 eV). It is found that the Raman intensities of R6G (1×10^{-5} M) adsorbed on $Mo_{4/3}B_2$ MBene under the excitation of 633 nm (1.96 eV) is much lower than that under the excitation at 532 nm (Fig. 5f), which is likely caused by the mismatch between the excitation laser of 633 nm and the HOMO–LUMO energy gap of the molecule (Fig. S5 in the ESI†).[46] Additionally, the PICT processes from the Fermi level of MBene to the LUMO of R6G (B-term), and from the HOMO of R6G to the Fermi level of MBene (C-term) are allowed (Fig. 5e). These PICT processes would borrow intensities from the nearby molecular resonance through the Herzberg–Teller vibronic coupling, magnifying the Raman scattering cross-section of molecule consequently.[52] Plasmon-free SERS substrates have unique molecular selectivity.[16,53] Furthermore, taking 4-mercaptopyridine (4-MPy) as a probe molecule, its HOMO and LUMO levels are located at −9.7 eV

This journal is © The Royal Society of Chemistry 2023

Published on 06 Genver 2023. Downloaded on 2025-08-25 06:33:52.

and −5.6 eV, respectively.[54] Under the excitation of 532 nm laser (2.33 eV), the molecular resonance is ruled out (the energy gap between HOMO and LUMO of 4-MPy is ~4.1 eV), the PICT process from the HOMO of 4-MPy to the Fermi level of MBene is not allowed (Fig. S6 in the ESI†). Only the PICT process between the Fermi level of MBene and the LUMO of 4-MPy could occur. Therefore, the 4-MPy molecule adsorbed on 2D $Mo_{4/3}B_2$ showed a poor SERS signal (Fig. S7 in the ESI†). This selective Raman enhancement further demonstrates that the SERS mechanism of 2D $Mo_{4/3}B_2$ is CM-dominated.

To further understand the efficient PICT processes in $Mo_{4/3}B_2$-molecule system, the Raman spectra and intensity columns of R6G (1×10^{-4} M) collected on bulk MoB and 2D $Mo_{4/3}B_2$ Mbene are shown in Fig. 5g and Fig. S8, respectively, in the ESI.† The characterizations of bulk MoB are shown in Fig. S9 and S10 in the ESI.† Notably, the SERS performance of 2D $Mo_{4/3}B_2$ MBene is superior to that of bulk MoB. The enhanced Raman peak P1 of R6G on 2D $Mo_{4/3}B_2$ MBene shows ~116 times higher intensity than that on bulk MoB. Furthermore, the lowest detectable concentration of R6G on 2D $Mo_{4/3}B_2$ MBene is 1×10^{-9} M (Fig. 3b), which is 5 orders of magnitude lower than that of bulk MoB (1×10^{-4} M, Fig. S11 in the ESI†). Other molecules, such as CV and MG, adsorbed on 2D $Mo_{4/3}B_2$ MBene were also observed with stronger SERS intensities compared to bulk MoB (Fig. S12, in the ESI†). DFT calculations were conducted to explain why the 2D $Mo_{4/3}B_2$ MBene shows superior SERS activity to the bulk MoB. According to Fermi's golden rule, the electron transition probability can be described as $w_{ab} = \frac{2\pi}{\hbar}|\langle b|M|a\rangle|^2 g_b$, in which $\hbar$ is the reduced Planck constant, $|a\rangle$ and $|b\rangle$ are the initial and final states for the charge transition, M is the interaction operator of the two states, and g_b is the DOS of the final state.[52] Therefore, plenty of allowed energy states near the Fermi level will give rise to a high electron transition probability between the adsorbed molecules and the SERS substrates. As shown in Fig. 5h, 2D $Mo_{4/3}B_2$ MBene possesses a higher electronic DOS value near the Fermi level than that of the bulk MoB. The larger DOS value is beneficial to the improvement of the electron transition probability rate, leading to a remarkable Raman enhancement effect on the 2D $Mo_{4/3}B_2$ MBene. Previous studies have demonstrated that vacancies play an important role in enhancing the non-noble-metal SERS effect.[55,56] Furthermore, we calculated the DOS of 2D Mo_2B_2, $Mo_{4/3}B_2$, and $Mo_{2/3}B_2$ MBenes. As shown in Fig. 5i, the DOS of 2D molybdenum boride Mbenes near the Fermi level follows the sequence of $Mo_{4/3}B_2$ > $Mo_{2/3}B_2$ > Mo_2B_2. Therefore, we believe that the presence of ordered metal vacancies in 2D molybdenum boride MBenes could improve their SERS sensitivity. Higher SERS sensitivity could be achieved by regulating the number of metal vacancies.[57]

3. Conclusion

In summary, we developed a brand-new high-performance MBene SERS platform for the first time. 2D $Mo_{4/3}B_2$ MBene with ordered metal vacancies could be synthesized by selectively etching the Al and Y atoms from the in-plane chemically ordered $(Mo_{2/3}Y_{1/3})_2AlB_2$. The 2D $Mo_{4/3}B_2$ MBene substrate exhibits an ultrahigh Raman EF of 3.88×10^6 and an ultralow detection limit of 1×10^{-9} M, which is comparable to most of the semiconductor SERS-active materials and even plasmonic noble metals. The Raman enhancement mechanism of 2D $Mo_{4/3}B_2$ MBene substrate is mainly attributed to the efficient photoinduced charge transfer process between the adsorbed molecules and the MBene substrates. 2D $Mo_{4/3}B_2$ MBene possesses a more abundant electronic DOS near the Fermi level, presenting a Raman EF by up to 5 orders compared with bulk MoB. Consequently, 2D $Mo_{4/3}B_2$ MBene could accurately detect 7 types of trace chemical analytes. In addition, with ordered metal vacancies in 2D $Mo_{4/3}B_2$ MBene, uniform charge transfer sites are formed, resulting in superior signal uniformity with a relative standard deviation down to 6.0%. Our work not only extends SERS-active material to a brand-new realm of MBene substrate but also provides a novel strategy to design high-performance MBene-based SERS platforms.

4. Experimental section

4.1 Fabrication of 2D $Mo_{4/3}B_2$ MBene

2D $Mo_{4/3}B_2$ MBene was prepared by selective etching the Al and Y atoms from $(Mo_{2/3}Y_{1/3})_2AlB_2$. Typically, 1.0 g $(Mo_{2/3}Y_{1/3})_2AlB_2$ (200 mesh) was slowly added to 10 mL HF (40 wt%, Aladdin Regent Co. Ltd) and stirred for 3.5 h at 35 °C. Afterwards, the etched sample was centrifuged at 5000 rpm for 2 min and washed several times with deionized water until the pH value of the supernatant reached 7. Then, the multi-layered $Mo_{4/3}B_2$ MBene was obtained after drying in a vacuum oven at 60 °C for 12 h. The 2D $Mo_{4/3}B_2$ MBene was prepared by further delamination of multi-layered $Mo_{4/3}B_2$ MBene. The obtained multi-layer $Mo_{4/3}B_2$ MBene was dispersed in 15 mL of TBAOH (20 wt%, Shanghai Macklin Biochemical Co. Ltd) and stirred for 2 min. Then, the sample was centrifuged at 6000 rpm for 2 min and washed three times with deionized water to remove the residual TBAOH. After decanting the supernatant, 10 mL of deionized water was added to the intercalated powders. Then, the mixture was shaken for 10 min and centrifuged at 6000 rpm for 2 min. Finally, the stable 2D $Mo_{4/3}B_2$ MBene colloidal suspension was obtained.

4.2 Characterization

XRD patterns were recorded on a Rigaku Smartlab X-ray diffractometer. XPS spectra were acquired on a Thermofisher ESCALAB 250Xi apparatus. We used argon ions to remove the surface oxide layer of the sample before the XPS measurements. TEM images were obtained on an FEI TEM (Talos F200X) instrument. SEM images and the corresponding elemental mapping images were obtained on a FEIXL-30 SEM. The thickness of the samples was measured on an atomic force microscope (AFM, BRUKER Dimension Icon). The UV-vis absorption spectra were recorded with a spectrophotometer (Shimadzu, UV-2600).

Published on 06 Genver 2023. Downloaded on 2025-08-25 06:33:52.

4.3 Raman measurements

The $Mo_{4/3}B_2$ dispersion was deposited on the Si substrate and then dried in ambient air. Before the Raman measurements, $Mo_{4/3}B_2$ MBene substrates were immersed in the probe molecule solutions for 1 h and then dried using N_2. Raman measurements were conducted on a Jobin Yvon Lab RAM HR800 Raman spectrometer with laser excitations of 532 and 633 nm. During the measurements, the laser power on the sample surface was 250 μW and all the integral times were 5 s.

4.4 First-principles calculations

All our first-principles calculations were carried out within the framework of DFT, as implemented in the Vienna *ab initio* simulation package, to obtain insights into the equilibrium structure and electronic properties of $Mo_{4/3}B_2$ and MoB. Periodic boundary conditions were used for the 2D structures throughout the study and a vacuum spacing of 30 Å was employed to eliminate the interactions between layers. The vdW correction of the DFT-D2 method was considered when dealing with multilayers. The reciprocal space was sampled by a fine grid of 6 × 6 × 1 *k*-points in the Brillouin zone. The projector-augmented-wave pseudopotentials and the Perdew–Burke–Ernzerhof exchange–correlation approximation were used. The electronic wave function was expanded on a plane-wave basis set with a cutoff energy of 550 eV. A total energy difference between subsequent self-consistency iterations below 10^{-5} eV was used as the criterion for reaching self-consistency. All geometries were optimized using the conjugate-gradient method until none of the residual Hellmann–Feynman forces exceeded 10^{-2} eV $Å^{-1}$.

Author contributions

Leilei Lan: conceptualization, methodology, validation, investigation, funding acquisition, writing – original draft. Xingce Fan: investigation, funding acquisition, writing – original draft. Caiye Zhao: conceptualization, investigation, resources. Juan Gao: writing – review and editing. Zhongwei Qu: investigation, resources. Wenzhe Song: investigation. Haorun Yao: writing – review and editing. Mingze Li: validation, resources. Teng Qiu: conceptualization, methodology, writing – review and editing, supervision, project administration, funding acquisition.

Conflicts of interest

The authors declare no conflicts of interest.

Acknowledgements

This work was supported by the National Natural Science Foundation of China (Grant No. 11874108) and the Fundamental Research Funds for the Central Universities (Grant No. 2242021R41069 and 2242022k30008). L. L. acknowledges the support funded by the Scientific Research Foundation for High-level Talents of Anhui University of Science and Technology (2022yjrc91). X. F. acknowledges the support received from the China Postdoctoral Science Foundation (Grant No. 2021M700773) and Jiangsu Planned Projects for Postdoctoral Research Funds (Grant No. 2021K509C).

References

1 Y. H. Wang, S. S. Zheng, W. M. Yang, R. Y. Zhou, Q. F. He, P. Radjenovic, J. C. Dong, S. N. Li, J. X. Zheng, Z. L. Yang, G. Attard, F. Pan, Z. Q. Tian and J. F. Li, *Nature*, 2021, **600**, 81.
2 L. Shi, M. M. Liu, L. M. Zhang and Y. A. Tian, *Angew. Chem., Int. Ed.*, 2022, **61**, e202117125.
3 R. Zhang, Y. Zhang, Z. C. Dong, S. Jiang, C. Zhang, L. G. Chen, L. Zhang, Y. Liao, J. Aizpurua, Y. Luo, J. L. Yang and J. G. Hou, *Nature*, 2013, **498**, 82–86.
4 W. Lee, B. H. Kang, H. Yang, M. Park, J. H. Kwak, T. Chung, Y. Jeong, B. K. Kim and K. H. Jeong, *Nat. Commun.*, 2021, **12**, 159.
5 X. X. Han, W. Ji, B. Zhao and Y. Ozaki, *Nanoscale*, 2017, **9**, 4847–4861.
6 L. L. Lan, H. R. Yao, G. Q. Li, X. C. Fan, M. Z. Li and T. Qiu, *Nano Res.*, 2022, **15**, 3794–3803.
7 L. L. Lan, Y. M. Gao, X. C. Fan, M. Z. Li, Q. Hao and T. Qiu, *Front. Phys.*, 2021, **16**, 43300.
8 L. Tao, K. Chen, Z. F. Chen, C. X. Cong, C. Y. Qiu, J. J. Chen, X. M. Wang, H. J. Chen, T. Yu, W. G. Xie, S. Z. Deng and J. B. Xu, *J. Am. Chem. Soc.*, 2018, **140**, 8696–8704.
9 X. Ling, L. M. Xie, Y. Fang, H. Xu, H. L. Zhang, J. Kong, M. Dresselhaus, J. Zhang and Z. F. Liu, *Nano Lett.*, 2010, **10**, 553–561.
10 Y. Yin, P. Miao, Y. M. Zhang, J. C. Han, X. H. Zhang, Y. Gong, L. Gu, C. Y. Xu, T. Yao, P. Xu, Y. Wang, B. Song and S. Jin, *Adv. Funct. Mater.*, 2017, **27**, 1606694.
11 G. Song, W. B. Gong, S. Cong and Z. G. Zhao, *Angew. Chem., Int. Ed.*, 2021, **60**, 5505–5511.
12 X. T. Wang, W. X. Shi, S. X. Wang, H. W. Zhao, J. Lin, Z. Yang, M. Chen and L. Guo, *J. Am. Chem. Soc.*, 2019, **141**, 5856–5862.
13 H. Z. Sun, W. B. Gong, S. Cong, C. L. Liu, G. Song, W. B. Lu and Z. G. Zhao, *ACS Appl. Mater. Interfaces*, 2022, **14**, 2326–2334.
14 B. Soundiraraju and B. K. George, *ACS Nano*, 2017, **11**, 8892–8900.
15 Y. S. Peng, C. L. Lin, L. Long, T. Masaki, M. Tang, L. L. Yang, J. J. Liu, Z. R. Huang, Z. Y. Li, X. Y. Luo, J. R. Lombardi and Y. Yang, *Nano-Micro Lett.*, 2021, **13**, 52.
16 M. Z. Li, Y. J. Wei, X. C. Fan, G. Q. Li, Q. Hao and T. Qiu, *Nano Res.*, 2022, **15**, 637–643.
17 Z. H. Zheng, S. Cong, W. B. Gong, J. N. Xuan, G. H. Li, W. B. Lu, F. X. Geng and Z. G. Zhao, *Nat. Commun.*, 2017, **8**, 1993.

 This journal is © The Royal Society of Chemistry 2023

Published on 06 Genver 2023. Downloaded on 2025-08-25 06:33:52.

18 L. L. Lan, X. C. Fan, S. B. Yu, J. Gao, C. Y. Zhao, Q. Hao and T. Qiu, *ACS Appl. Mater. Interfaces*, 2022, **14**, 40427–40436.
19 M. Z. Li, Y. M. Gao, X. C. Fan, Y. J. Wei, Q. Hao and T. Qiu, *Nanoscale Horiz.*, 2021, **6**, 186–191.
20 H. Z. Sun, G. Song, W. B. Gong, W. B. Lu, S. Cong and Z. G. Zhao, *Nano Res.*, 2022, **15**, 5347–5354.
21 Z. H. Hu, Z. T. Wu, C. Han, J. He, Z. H. Ni and W. Chen, *Chem. Soc. Rev.*, 2018, **47**, 3100–3128.
22 J. Seo, Y. Kim, J. Lee, E. Son, M. H. Jung, Y. M. Kim, H. Y. Jeong, G. Lee and H. Park, *J. Mater. Chem. A*, 2022, **10**, 13298–13304.
23 Q. Lv, J. Y. Tan, Z. J. Wang, L. X. Yu, B. Liu, J. H. Lin, J. Li, Z. H. Huang, F. Y. Kang and R. T. Lv, *Adv. Funct. Mater.*, 2022, **32**, 2200273.
24 Z. L. Guo, J. Zhou and Z. M. Sun, *J. Mater. Chem. A*, 2017, **5**, 23530–23535.
25 G. Bhaskar, V. Gvozdetskyi, M. Batuk, K. M. Wiaderek, Y. Sun, R. H. Wang, C. Zhang, S. L. Carnahan, X. Wu, R. A. Ribeiro, S. L. Bud'ko, P. C. Canfield, W. Y. Huang, A. J. Rossini, C. Z. Wang, K. M. Ho, J. Hadermann and J. V. Zaikina, *J. Am. Chem. Soc.*, 2021, **143**, 4213–4223.
26 L. T. Alameda, P. Moradifar, Z. P. Metzger, N. Alem and R. E. Schaak, *J. Am. Chem. Soc.*, 2018, **140**, 8833–3340.
27 J. J. Wang, T. N. Ye, Y. T. Gong, J. Z. Wu, N. X. Miao, T. Tada and H. Hosono, *Nat. Commun.*, 2019, **10**, 2284.
28 X. Y. Guo, S. R. Lin, J. X. Gu, S. L. Zhang, Z. F. Chen and S. P. Huang, *Adv. Funct. Mater.*, 2021, **31**, 2008056.
29 H. M. Zhang, F. Z. Dai, H. M. Xiang, X. H. Wang, Z. L. Zhang and Y. C. Zhou, *J. Mater. Sci. Technol.*, 2019, **35**, 1593–1600.
30 D. Y. Chen, Z. K. Jin, B. Zhao, Y. S. Wang and Q. J. He, *Adv. Mater.*, 2021, **33**, 2008089.
31 V. G. Nair, M. Birowska, D. Bury, M. Jakubczak, A. Rosenkranz and A. M. Jastrzebska, *Adv. Mater.*, 2022, **34**, 2108840.
32 M. Dahlqvist, Q. Z. Tao, J. Zhou, J. Palisaitis, P. O. A. Persson and J. Rosen, *J. Am. Chem. Soc.*, 2020, **43**, 18583–18591.
33 J. Zhou, J. Palisaitis, J. Halim, M. Dahlqvist, Q. Z. Tao, I. Persson, L. Hultman, P. O. A. Persson and J. Rosen, *Science*, 2021, **373**, 801.
34 Q. Z. Tao, M. Dahlqvist, J. Lu, S. Kota, R. Meshkian, J. Halim, J. Palisaitis, L. Hultman, M. W. Barsoum, P. O. A. Persson and J. Rosen, *Nat. Commun.*, 2017, **8**, 14949.
35 R. Meshkian, M. Dahlqvist, J. Lu, B. Wickman, J. Halim, J. Thornberg, Q. Z. Tao, S. X. Li, S. Intikhab, J. Snyder, M. W. Barsoum, M. Yildizhan, J. Palisaitis, L. Hultman, P. O. A. Persson and J. Rosen, *Adv. Mater.*, 2018, **30**, 1706409.
36 M. Naguib, O. Mashtalir, J. Carle, V. Presser, J. Lu, L. Hultman, Y. Gogotsi and M. W. Barsoum, *ACS Nano*, 2012, **6**, 1322–1331.
37 K. Hantanasirisakul and Y. Gogotsi, *Adv. Mater.*, 2018, **30**, 1804779.
38 R. Wu, H. K. Xu, Y. W. Zhao, C. Y. Zha, J. Deng, C. Y. Zhang, G. Lu, T. S. Qin, W. Wang, Y. Yin, C. Zhu, L. Wang, G. Ouyang and W. Huang, *Energy Storage Mater.*, 2020, **32**, 216–224.
39 S. Vinoth, H. T. Das, M. Govindasamy, S. F. Wang, N. S. Alkadhi and M. Ouladsmane, *J. Alloys Compd.*, 2021, **877**, 160192.
40 X. C. Fan, P. H. Wei, G. Q. Li, M. Z. Li, L. L. Lan, Q. Hao and T. Qiu, *ACS Appl. Mater. Interfaces*, 2021, **13**, 51618–51627.
41 Q. Q. Zhang, X. S. Li, Q. Ma, Q. Zhang, H. Bai, W. C. Yi, J. Y. Liu, J. Han and G. C. Xi, *Nat. Commun.*, 2017, **8**, 14903.
42 J. Lin, Y. Shang, X. X. Li, J. Yu, X. T. Wang and L. Guo, *Adv. Mater.*, 2017, **29**, 1604797.
43 W. Ji, L. F. Li, W. Song, X. N. Wang, B. Zhao and Y. Ozaki, *Angew. Chem., Int. Ed.*, 2019, **58**, 14452–14456.
44 J. B. Li, W. C. Yi, M. Yin, H. F. Yang, J. F. Li, Y. H. Li, Z. W. Jiao, H. Bai, M. Q. Zou and G. C. Xi, *ACS Nano*, 2022, **16**, 1160–1169.
45 H. Z. Sun, S. Cong, Z. H. Zheng, Z. Wang, Z. G. Chen and Z. G. Zhao, *J. Am. Chem. Soc.*, 2019, **141**, 870–878.
46 L. L. Yang, Y. S. Peng, Y. Yang, J. J. Liu, H. L. Huang, B. H. Yu, J. M. Zhao, Y. L. Lu, Z. R. Huang, Z. Y. Li and J. R. Lombardi, *Adv. Sci.*, 2019, **6**, 1900310.
47 Y. C. Ge, F. Wang, Y. Yang, Y. Xu, Y. Ye, Y. Cai, Q. W. Zhang, S. Y. Cai, D. F. Jiang, X. H. Liu, B. Liedberg, J. Mao and Y. Wang, *Small*, 2022, **18**, 2107027.
48 G. Demirel, R. L. M. Gieseking, R. Ozdemir, S. Kahmann, M. A. Loi, G. C. Schatz, A. Facchetti and H. Usta, *Nat. Commun.*, 2019, **10**, 5502.
49 Z. H. Lei, X. K. Zhang, Y. Zhao, A. X. Wei, L. L. Tao, Y. B. Yang, Z. Q. Zheng, L. Tao, P. Yu and J. B. Li, *Nanoscale*, 2022, **14**, 4181–4181.
50 C. Liang, Z. A. Lu, M. Zheng, M. X. Chen, Y. Y. Zhang, B. Zhang, J. X. Zhang and P. Xu, *Nano Lett.*, 2022, **22**, 6590–6598.
51 Q. Q. Ding, J. Wang, X. Y. Chen, H. Liu, Q. J. Li, Y. L. Wang and S. K. Yang, *Nano Lett.*, 2020, **20**, 7304–7312.
52 X. J. Song, Y. Wang, F. Zhao, Q. C. Li, H. Q. Ta, M. H. Rummeli, C. G. Tully, Z. Z. Li, W. J. Yin, L. T. Yang, K. B. Lee, J. Yang, I. Bozkurt, S. W. Liu, W. J. Zhang and M. Chhowalla, *ACS Nano*, 2019, **13**, 8312.
53 S. X. Huang, X. Ling, L. B. Liang, Y. Song, W. J. Fang, J. Zhang, J. Kong, V. Meunier and M. S. Dresselhaus, *Nano Lett.*, 2015, **15**, 2892–2901.
54 N. J. Kim, J. Kim, J. B. Park, H. Kim, G. C. Yi and S. Yoon, *Nanoscale*, 2019, **11**, 45–49.
55 Y. N. Quan, X. H. Tang, W. Shen, P. H. Li, M. Yang, X. J. Huang and W. Q. Liu, *Adv. Opt. Mater.*, 2022, **23**, 2201395.
56 S. Cong, Y. Y. Yuan, Z. G. Chen, J. Y. Hou, M. Yang, Y. L. Su, Y. Y. Zhang, L. Li, Q. W. Li, F. X. Geng and Z. G. Zhao, *Nat. Commun.*, 2015, **6**, 7800.
57 I. R. Shein and A. L. Ivanovskii, *Phys. Rev. B: Condens. Matter Mater. Phys.*, 2006, **73**, 144108.